Journal of Energy Storage 36 (2021) 102388

Contents lists available at ScienceDirect

Journal of Energy Storage

journal homepage: www.elsevier.com/locate/est

A first principles framework to predict the transient performance of latent heat thermal energy storage

Kedar Prashant Shete *, S.M. de Bruyn Kops, Dragoljub (Beka) Kosanovic

Mechanical and Industrial Engineering, 219 Engineering Laboratory, University of Massachusetts, 160 Governors Drive, Amherst, MA 01003-2210, United States of America

ARTICLE INFO

Keywords:
Latent heat thermal energy storage
Melt fraction
Natural convection
Finite Volume Method

ABSTRACT

Thermal energy storage (TES) is increasingly recognized as an essential component of efficient Combined Heat and Power (CHP), Concentrated Solar Power (CSP), Heating Ventilation and Air Conditioning (HVAC), and refrigeration as it reduces peak demand while helping to manage intermittent availability of energy (e.g., from solar or wind). Latent Heat Thermal Energy Storage (LHTES) is a viable option because of its high energy storage density. Parametric analysis of LHTES in terms of dimensionless numbers is highly desired as a tool to model LHTES systems. One approach is to develop a model equation so as to minimize the error between the model and data obtained from experiments or simulations. While this approach can produce an accurate correlation applicable within the range of data used for its creation, it does not provide physical understanding of the rate-limiting process controlling the transient behavior of the device. In this paper we present an alternative approach whereby the potential rate-limiting processes are identified from first principles and then the key process is determined as a function of time as a LHTES device is charged. For example, in a simple geometry, the melt-fraction can be expected to vary linearly in time if the heat transfer rate is limited by natural convection of the phase changing material and we show it scales with the PCM Grashof number as Gr_p^1 and PCM Prandtl number as $Pr_p^{(1/3)}$. On the other hand, if surface area of solid PCM limits the heat transfer rate, the melt fraction increases asymptotically to reach full melting. The existence of these linear and asymptotic regions and the $Gr_p^1 Pr_p^{1/3}$ shape of the melt fraction curve is verified using our database of 64 simulations. Of practical importance in designing LHTES devices is the melt fraction at which the heat transfer rate ceases to be limited by convection, after which the heat storage rate deteriorates. For our geometry, this is found to be about 90%. This test case of our methodology shows the value of our approach, that predicting heat storage rate based on the rate-limiting physical phenomenon as a function of time is an effective approach to modeling LHTES devices.

1. Introduction

Thermal energy storage (TES) is increasingly recognized as an essential component of efficient combined heat and power (CHP), concentrated solar power (CSP), heating ventilation and air conditioning (HVAC), and refrigeration as it reduces peak demand while helping to manage intermittent availability of energy (e.g., from solar or wind). As discussed in more detail below, it has the potential to reduce energy consumption and reduce pollution generation by making existing technologies more efficient and by enabling the integration of renewable energy sources with minimum energy curtailment.

Given the thermo-physical properties of a heat storage material, it is straightforward to compute the amount of that material required to store a given amount of heat. The challenge is in designing a physical device that enables sufficiently high heat transfer rate for a practical system. If, for example, a TES is to be coupled with a CHP plant, the TES must be able to store and release heat at the time scale of the transients in the CHP system. Designing a TES system to meet this requirement is difficult because a very large number of parameters affect the heat transfer rate including the properties of the working fluids, the fluid dynamical regimes of those fluids when the system is operating, the geometry of the heat exchanger and storage device, and the operating conditions for the entire system. In this paper, we present an approach for dealing with this complexity. Our approach consists of systematically defining the relevant dimensionless parameters and then writing the relationships between these parameters based on physical understanding derived from theory and from the literature about TES systems. We apply it to the specific case of latent heat thermal energy

* Corresponding author.
E-mail addresses: kshete@umass.edu, kedar.kshete@gmail.com (K.P. Shete), debk@umass.edu (S.M. de Bruyn Kops), kosanovic@umass.edu (D. Kosanovic).

https://doi.org/10.1016/j.est.2021.102388
Received 28 October 2020; Received in revised form 5 February 2021; Accepted 6 February 2021
Available online 8 March 2021

Nomenclature

η	Melt fraction
ρ	Density
μ	Viscosity
β	Volumetric expansion coefficient
T	Temperature
u	Velocity
M	Mass
α	Thermal diffusivity
ν	Kinematic viscosity
q	Heat transfer rate into control volume
h	Mean heat transfer coefficient
D	Diameter
A_{mush}	Mushy zone constant
λ	Liquid fraction
τ	Generic dimensionless time
C_p	Specific heat capacity at constant pressure
l	Length
f	Heat transfer fluid (HTF)
p	Phase change material (PCM)
t	HTF tube
c	PCM container
i	Inner
o	Outer
in	Inlet
$mean$	Mean
fr	HTF Reynolds number
fp	HTF Prandtl number
pg	PCM Grashof number
pp	PCM Prandtl number
τ	Dimensionless time

storage (LHTES) to demonstrate how the approach can introduce physical understanding into relationships between parameters that have typically been studied empirically and, thereby, simplify the overall design process.

Applications that are improved significantly with thermal energy storage include concentrating solar power (CSP) plants; Denholm et al. [1] report round-trip efficiencies close to 100% when energy from CSP's is stored as thermal energy rather than electrical energy. They also report that "cold storage" enables extremely high efficiency of cooling systems by shifting demand to off-peak hours. Nithyanandam and Pitchumani [2], based on their study of charging and discharging cycles of a LHTES heat exchanger, emphasize the importance of LHTES for the effective functioning of CSP. Performance of cogeneration power plants also improves when they are combined with thermal energy storage [3,4]. Venkitaraj et al. [5] investigate experimentally the use of nano-particle enhanced LHTES for waste heat recovery from IC engines and observe up to 18% increase in the energy savings. In addition to improvements in energy efficiency, thermal energy storage can reduce emission of pollutants. For example, Li et al. [6] calculate the effect of a LHTES system used to recover waste heat from a heavy duty diesel engine and conclude a potential 40% improvement in engine warm up time during which the engine produces suboptimal emissions. Arbabzadeh et al. [7] report the huge potential impact of energy storage on decarbonization of electricity production by allowing electricity usage for heating and cooling to be synchronized with when renewable energy is available. Specifically, they conclude that, for the state of California, thermal energy storage can result in an 18% reduction in carbon dioxide emission and a 21% reduction in renewable energy curtailment, that is, the reduction of output of a renewable resource below what it could have otherwise produced. This reiterates the importance of using TES devices in energy systems.

LHTES has inherent advantages over other TES systems with respect to high storage density and heat transfer at constant temperature. High storage density might lead to smaller device sizes or lower costs, although we do not discuss those as they are beyond the scope of this paper. Thus, LHTES would appear to be a very attractive option for improving the energy efficiency and reducing emissions of a variety of types of power plants and engines. Indeed, Mongibello et al. [8] study two different types of thermal energy storage for residential micro-CHP systems and conclude that LHTES is preferred over sensible energy storage (such as hot water) in terms of cost and size. They also conclude that further analysis should be made, including of the long-term performance and degradation of these systems over time, in order to assess the convenience of using them for thermal energy storage. Johar et al. [9] implement a LHTES system within a micro-CHP plant and shows LHTES can be a viable option. They note, though, that improved design procedures and performance modeling of phase change heat exchangers are essential. Thus, we see that a modeling of the heat transfer rate in LHTES devices is valuable and needed.

Heat exchanger geometry is a crucial factor affecting the heat transfer rate of LHTES. Geometry parameters that have been studied include the inner and outer diameters in an annular geometry with PCM in the annulus and Heat transfer fluid (HTF) in the inner pipe [10,11], HTF pipe wall thickness [12] and diameter of the HTF pipe [13]. Adding fins in the PCM has been shown to improve charging rates, stored energy and melting front depth [11,13,14]. For a given percentage of fin material/metal inside the heat exchanger, a higher number of thinner fins lead to better heat transfer [14]. The overall configuration of the LHTES is also an important factor, and various configurations including a single HTF pipe inside an annular PCM container, multiple HTF tubes inside a PCM pipe, PCM modules floating inside an HTF container and direct contact between HTF and PCM have been studied [15]. The orientation of the device also affects its performance [11].

The thermophysical properties of the HTF and PCM such as thermal conductivity and specific heat capacity are also important parameters affecting the performance of LHTES [10,12,13,15,16]. Gasia et al. [15] conclude that an increase in specific heat capacity of HTF of 4.9 times and in thermal conductivity of HTF of 3 times improves the charging times by 44%. Materials such as paraffins have moderate energy storage density and low cost, but also have low thermal conductivity, which affects their utility as energy storage materials. Hydrated salts have larger thermal conductivity and large energy storage capacity, but their use is affected by other material properties like supercooling and phase segregation. The melting point is one of the most important characteristic in selecting a phase change material [16].

The HTF mass flow rate and temperature have a major effect on the LHTES performance because it is the HTF that determines the mean wall temperature of the HTF tube. This in turn affects natural convection in PCM, which is a key component of accurately modeling energy storage rates [17]. The effect of HTF mass flow rate and HTF temperature has been studied by a number of authors [11,17,18]. For example, a study conducted in terms of dimensionless parameters is that of Teamah et al. [18], who obtain a dependency of $FoRe^{0.8}\theta_m$ and $Ste(\rho C_p)^*$ for the total energy gain and concluded that the dependency of $Re^{0.8}$ originates from the turbulent convection coefficient correlation used within their finite difference calculation, which shows that if the energy available in the HTF is a limiting factor, the HTF Reynolds number shall have an effect on the energy storage rate. Understanding the effect of individual parameters on the performance and quantifying their importance relative to other parameters will greatly support the design process for LHTES devices [16]. Indeed, attempts have been made in recent research to apply battery characterization techniques to LHTES [19]. It is advantageous to have dimensionless results instead of purely experimental data pertaining to just one device [17].

The conjoined use of composite materials and novel LHTES designs can also have a marked effect on the heat transfer rate, especially in applications limited by availability of space. The addition of fins (more so with longer and thinner fins) is found to be a very effective way to maximize melting and solidification rates, but the fins have less of an effect on melting rates than on solidification rates due to the suppression of natural convection, which plays an important role in melting [20,21]. However, adding a metal foam structure instead of films, especially in the laminar regime is found to enhance melting rates due to the conductivity enhancement resulting from the metal foam being more prominent than the suppression of natural convection due to the foam [22]. The use of a composite foam-PCM structure is found to result in best cooling performance due to the high conductivity of the metal foam when the PCM is not melted, and the high heat absorption capacity of the PCM on the onset of melting [23]. Jiang and Qu [24] investigated the performance of a PCM + heat pipe device to cool a Li-ion battery and found that the addition of heat pipe enables the device to cycle longer (by dissipating latent heat from the PCM) and cool the battery more effectively. The optimal value of the volume fraction and porosity of the added nano-particles and metal foams to a LHTES device under laminar conditions is found to be 0.01 and 0.95 respectively [25].

It is apparent that the foundation has been laid for understanding the individual factors affecting heat transfer rate in LHTES systems. Less progress has been made on combining these individual factors to form a complete set of relevant dimensionless parameters suitable for robust modeling and design guidance for creating LHTES systems having sufficiently high heat transfer rates for commercial applications.

2. Hypothesis for transient behavior of LHTES

A variety of configurations exist for LHTES systems, but they have certain common elements. Typical LHTES devices consist of a heat exchanger with a heat transfer fluid (HTF), such as oil, pumped across one side of a solid interface and a PCM driven by natural convection on the other side. Starting from the solid state in the PCM, introduction of heat to the system via the HTF melts some of the PCM and buoyancy begins to drive flow. Three factors quantify the practical performance of an energy storage/LHTES device: the charging rate, the discharging rate and the storage capacity. In a LHTES device, the storage capacity is very simple to predict because it is directly proportional to the mass of the of PCM in the system. The charging and discharging rates are more difficult to predict because, as reviewed in the previous section, they depend on the geometry of the heat transfer surface, the thermophysical properties of the fluids, and the operating conditions of the entire system. Here we consider only the charging rate and leave the discussion of the discharging rate to a future study.

A common approach to modeling the charging rate is to fit an assumed function to experimental or numerical data. For example, Rathod and Jyotirmay [26] use polynomial regression to describe the melting time as a function of the Reynolds number in the HTF, the Stefan number of the PCM and the ratio of initial temperature of the PCM and inlet temperature of the HTF. Correlations predicting the transient behavior of LHTES devices are considered more valuable than those predicting endpoint melting time. Diarce et al. [27] conduct such a study for a plate based LHTES system. They identify a critical Fourier number corresponding to 95% melted PCM, and assume a product of power-law relationship to fit the Fourier number as a function of the Biot number, the Stefan number and two dimensionless temperature constants. This approach can produce effective empirical correlations over the range of data used for regression, but offer limited insight into the transient behavior of the system and the natural convection flow physics.

We proceed using an alternative, first principles approach in order to hypothesize the transient behavior of an LHTES, which begins with identifying the dimensional system parameters expected to be important for the performance of LHTES systems. We note that the number of parameters affecting LHTES system performance is extremely large, tabulated in Table A.6. For example, the macroscopic geometry of the device can be quite complicated and, e.g., microscopic geometry of the heat transfer surfaces is a topic onto itself. So, as an example, we pick a vertical annular geometry of smooth-walled tubes with the HTF in the inner tube and PCM in the annulus. Next we apply the Buckingham Pi theorem to determine the minimum number of dimensionless groups given the dimensional parameters in Table A.6 and the assumption that mass, length, time, and temperature are independent dimensions. This leads us to expect 12 dimensionless parameters. Given the expected number of groups and the well-established definitions of many of them, we arrive at the dimensionless groups in Table 1.

The physical quantity of interest that defines the heat transfer rate in an LHTES system is the rate of change of the melt fraction. The HTF transports energy into the system, which is then transferred to other system components. Let the total heat transfer rate to the system be denoted by q_f, which is equal to the heat transfer out of the control volume HTF. This heat is then distributed between the PCM (q_p), HTF tube (q_t) and PCM container (q_c). There will be a transient as the temperatures of the PCM and heat transfer surfaces adjust to the melting point of the PCM. Once this transient is finished, q_t and q_c are expected to be small compared to q_p due to the high volume and the high heat capacity of the PCM. q_p can be further split into two components, the sensible heating rate q_{ps} which causes temperature rise in the PCM and the latent heating rate q_{pl} which causes melting of the PCM. q_{ps} is typically smaller than q_{pl} due to reasons similar as above; the latent heat capacity of the PCM L is two orders of magnitude higher than the sensible heat capacity Cp_p. In some cases, q_{ps} can be as high as 10% to 30% of the total heat stored. The heat transfer rate balance can be written as

$$\begin{aligned} q_f &= q_p + q_t + q_c \\ &= q_{pl} + q_{ps} + q_t + q_c + q_{loss} \end{aligned} \tag{1}$$

where if the device walls are insulated, q_{loss}, the heat lost to the environment from the surface of the device will be small. Out of these, q_{pl} is of particular interest as it represents high quality energy available at a fixed temperature. The integral of q_{pl} from the onset of melting to the current time is related to the melted fraction of PCM (η) by (2), where η is defined as the mass of melted PCM to the total mass of PCM.

$$q_{pl} = M_p L \frac{d\eta}{dt} \tag{2}$$

$$\eta = \frac{1}{M_p L} \int_0^t q_{pl} dt \tag{3}$$

η can be written as a function of all the parameters in Table A.6. For example, for the four parameter case described here,

$$\eta = \eta(t, u_f, k_f, k_p, T_{in}) \tag{4}$$

We begin by examining η as a function of time in the multi-dimensional space defined Gr_p, Pr_p, Re_f and Pr_f. The dimensionless groups Re_f, Gr_p, Pr_p and Pr_f correspond to u_f, T_{in}, k_p and k_f respectively. Table 2 shows the parameters considered in this study, corresponding dimensionless numbers and symbols. The melt fraction η has been used previously in literature as a function of dimensional time. For consistency, we denote the equivalent of η that accepts a generic dimensionless time τ as an argument, by η_τ. The goal is to find $\eta_\tau = \eta_\tau(\tau)$ with the τ defined in terms of a physically relevant time scale. If we are successful in this then the curves for $\eta_\tau(\tau)$ corresponding to different values of the parameter being varied will collapse to a single curve. In this section, we attempt to define a suitable τ based on the flow physics and observations from literature. A general dimensionless timescale can be defined as follows -

$$\tau = \tau(Fo_p, Gr_p, Pr_p, Re_f, Pr_f) \tag{5}$$

where Fo_p is the PCM Fourier number defined in Table 1. For brevity, we also introduce a shorthand notation for a one dimensional slice

Table 1
Non-Dimensional groups affecting heat transfer rates in LHTES devices. The independent groups corresponding to parameters in A.6 have been boxed. Other dependent groups like the Rayleigh number have been mentioned due to their importance in literature.

Numbers	HTF	PCM	HTF tube	PCM container
Reynolds number (Re)	$\boxed{\rho_f D_t u_f/\mu_f}$	–	–	–
Fourier number (Fo)	–	$\boxed{\alpha_p t/(D_{co}-D_{ci})^2}$	–	–
Prandtl number (Pr)	$\boxed{Cp_f\mu_f/k_f}$	$\boxed{Cp_p\mu_p/k_p}$	–	–
Péclet number (Pe)	$D_t u_f/\alpha_f$	–	–	–
Grashof number (Gr)	–	$\boxed{g\beta_p(D_{co}-D_{ci})^3(T_{mci}-T_{mean})/\nu_p^2}$	–	–
Rayleigh number (Ra)	–	$g\beta_p(D_{co}-D_{ci})^3(T_{mci}-T_{mean})/\nu_p\alpha_p$	–	–
Aspect ratio (AR)	–	–	$\boxed{l_t/D_t}$	$\boxed{l_c/(D_{co}-D_{ci})}$
Stefan number (Ste)	–	$\boxed{Cp_p(T_{mci}-T_{mean})/L}$	–	–
Biot number (Bi)	–	–	$\boxed{h_f(D_{ci}-D_t)/k_t}$	–
Nusselt number (Nu)	$\boxed{h_f D_t/k_f}$	$\boxed{h_p D_{ci}/k_p}$	–	–
Melting to heat transfer timescale	–	$\boxed{\Delta t_s/t \approx 0}$	–	–

Table 2
System parameters being varied in this study and the corresponding dimensionless numbers. A larger but not exhaustive list of parameters that can be varied has been given in table Table A.6.

Parameter	Symbol	Dimensionless number	Description
HTF inlet temperature	T_{in}	Gr_p	This determines the maximum temperature difference available for natural convection in the PCM. It corresponds to the Grashof number in the PCM.
PCM thermal conductivity	k_p	Pr_p	Corresponds to the Prandtl number in the PCM
HTF inlet velocity	u_f	Re_f	Determines the amount of energy available from the HTF, corresponds to the HTF Reynolds number
HTF thermal conductivity	k_f	Pr_f	Corresponds to the Prandtl number in the HTF

through τ, where all parameters except one are kept constant. For example, if all parameters except the PCM Grashof number Gr_p were held constant, τ would be given as

$$\tau|_{Re_f,Pr_f,Pr_p} = \tau_{pg} \tag{6}$$

where the subscript p denotes PCM and the additional subscript g denotes that the Grashof number is the variable in question.

Natural convection in the PCM is a known bottleneck for heat transfer in LHTES devices. The reasons for that are as follows: Even though the flow of HTF and its conductivity govern how much energy is available to the PCM, its effect is to raise the mean PCM wall temperature T_{mci} to T_{in} and determine whether the PCM melts. When this is achieved, the heat transfer rate is limited by the natural convection in the PCM. Thus, there must exist values of Re_f and Pr_f at which the heat transfer is not limited by the availability of energy in the HTF. If those values are achieved, Re_f and Pr_f will drop out of the general timescale in (5) and we will get τ only as a function of Gr_p and Pr_p. Based on the literature reviewed in Section 1, we hypothesize τ to scale as

$$\tau|_{Re_f,Pr_f} = Pr_p^{1/3} Gr_p Fo_p \tag{7}$$

for fixed Re_f and Pr_f indicated by the subscripts $Re_f, Pr_f = constant$. The Grashof number scaling hypothesized in (7) is consistent with what Jany and Bejan [28] observed by scaling analysis for mixed conduction–convection flow regimes in an enclosure with laminar flow. The Prandtl number scaling hypothesized here is consistent with the $Pr^{1/3}$ scaling observed in laminar forced convection with uniform heat flux, and we address our reasons for making this assumption in Section 4.2.

The structure of η is hypothesized to contain a linear region, based on the terms in (7). Let us now consider the limits on η for which this is expected to happen, and the structure of η outside these limits, which we expect to be asymptotic in behavior. The melt fraction at the transition between these regions is termed as the *transition melt fraction*, denoted by $\eta_{critical}$. The time at which $\eta_{critical}$ occurs is denoted by $\tau_{critical}$. We elaborate in Sections 2.1 and 2.2 on why each region can be expected from physical reasoning.

2.1. Linear region

If the flow of HTF is sufficient and does not limit the transport of heat into the device, the variation in the mean wall temperature T_{mci} is expected to be small. In the PCM, q_p, is proportional to the temperature difference $T_{mci}-T_{mean}$, of which T_{mean} is a constant and variations in T_{mci} are expected to be small compared to the aforementioned temperature difference. After an initial transient, q_{pl} is the major component of q_p. The melt fraction η, which is proportional to integral of q_{pl} as shown in (2), is expected be linear with time. At $\eta_{critical}$, the quantity of solid PCM gets small such that the characteristic temperature difference in the PCM changes to $T_{mci} - T_p$, where T_p is the mean temperature of the PCM and is approximately equal to the far field temperature. As the remaining quantity of solid PCM is small, T_p is expected to rise inverse-exponentially, which should result in the asymptotic behavior of η, as explained in the following section.

2.2. Asymptotic region

To obtain uncluttered equations, terms expected to be constant have been grouped into numbered constants for brevity. Let the mass of solid PCM at the time η reaches $\eta_{critical}$ be m_{pcm}, and let its surface area be a_{pcm}. Let the heat transfer coefficient on the solid liquid interface be h_{pcm}. Fig. 1 shows a representation of the variables of interest.

After η reaches a critical fraction $\eta_{critical}$, the mass of solid PCM is small and the characteristic temperature difference is closer to $T_{mci}-T_p$ rather than $T_{mci}-T_{mean}$. The configuration is shown in a schematic form in Fig. 1 along with the notation used in the following discussion In this

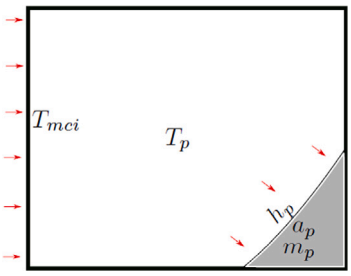

Fig. 1. The variables for the asymptotic region of η. The interface between m_{pcm} and the liquid is an arbitrarily drawn curve.

regime, there is limited contact area between the liquid and the solid and so most of the heat transferred from the HTF to the PCM raises the temperature of the PCM. With this approximation,

$$\begin{aligned} q_p = M_p C p_p \frac{dT_p}{dt} &= h_p A_p (T_{mci} - T_p) \\ \Rightarrow \frac{d(T_{mci} - T_p)}{dt} &= -\frac{h_p A_p}{M_p C p_p}(T_{mci} - T_p) \\ \Rightarrow \frac{d(T_{mci} - T_p)}{T_{mci} - T_p} &= -c_2' dt \\ \Rightarrow ln(T_{mci} - T_p) &= -c_2' t + c_1 \\ \Rightarrow T_p &= T_{mci} - c_2 e^{(-c_2' t)} \end{aligned} \tag{8}$$

In short, the PCM acts as a lumped capacitance [29, eq. 5.8a] because the mass of the solid PCM is insufficient to affect T_p. To simplify, we combine terms that are approximately constant into the coefficients c_1, c_2, c_2'. The prime notation denotes constants that carry forward into the final expression given in (11).

Assuming that the remaining solid PCM is at melting temperature and there is no significant sensible heating of the residual solid, the heat transfer to the solid PCM is

$$\begin{aligned} q_{pl} = L\frac{dm_{pcm}}{dt} &= h_{pcm} A_{pcm}(T_p - T_{mean}) \\ \Rightarrow \frac{d(1-\eta)}{dt} &= \frac{h_{pcm} A_{pcm}}{L M_p}(T_p - T_{mean}) \, . \end{aligned} \tag{9}$$

The area A_{pcm} depends on the mass of solid PCM and can be calculated if the shape of m_{pcm} and its density is known. Since the PCM is close to the melting temperature, the density can be considered to be a constant. At constant density, if m_{pcm} is a sphere, A_{pcm} is proportional to $m_{pcm}^{2/3}$. In general, A_{pcm} is proportional to m_{pcm}^{γ} where γ is some real number less than 1, expected to be constant if the melting front geometry and density do not change in the duration of the exponential melting region. Substituting this and (8) into (9) yields

$$\begin{aligned} \frac{d(1-\eta)}{dt} &= \frac{c_3 h_{pcm} m_{pcm}^{\gamma}}{L M_p}(T_p - T_{mean}) \\ \Rightarrow \frac{d(1-\eta)}{dt} &= \frac{c_3 h_{pcm}(1-\eta)^{\gamma}}{L M_p^{1-\gamma}}(T_p - T_{mean}) \\ \Rightarrow \frac{d(1-\eta)}{(1-\eta)^{\gamma}} &= \frac{c_3 h_{pcm}}{L M_p^{1-\gamma}}(T_p - T_{mean})dt \\ &= c_5\left((T_{mci} - T_{mean}) - c_2 e^{(-c_2' t)}\right)dt \\ &= c_5(T_{mci} - T_{mean})dt - c_2 c_5 e^{(-c_2' t)}dt \\ \Rightarrow \frac{(1-\eta)^{\gamma+1}}{\gamma+1} &= c_5(T_{mci} - T_{mean})t + c_6 e^{(-c_2' t)} + c_7 \\ \Rightarrow 1 - \eta &= \left(c_7' + c_5'(T_{mci} - T_{mean})t + c_6' e^{(-c_2' t)}\right)^{\frac{1}{\gamma+1}} \end{aligned} \tag{10}$$

From this we conclude that the function form for $\eta(t)$ in the asymptotic regions should be

$$\eta = 1 - \left(c_7' + c_5'(T_{mci} - T_{mean})t + c_6' e^{(-c_2' t)}\right)^{\frac{1}{\gamma+1}} \, . \tag{11}$$

In order to confirm the validity of our hypothesis, we conduct simulations of our geometry using the Finite Volume Method (FVM) for a parameter space described in Section 4. In the following section, we provide some details about our numerical method.

3. Numerical simulations approach

To verify our hypothesis in Section 2, we seek benchmark simulations that are free from models. In practice, some modeling is inherent in simulations, starting with the continuum approximation, which omits molecular effects inherent in the phase change process. Our approach is to limit the modeling in the simulations to: 1. The HTF is incompressible and Newtonian. 2. The initial temperature of the entire unit is uniform and the PCM is in the solid phase 3. The thermophysical properties of the liquid HTF, the PCM and the container are constant except for the density of the PCM. 4. The density changes in the PCM and their scaling height are small so that the non-hydrostatic Boussinesq approximation is applicable. 5. The kinetic and thermal energies of the PCM are decoupled. 6. The equations of motion for the liquid and solid phases of the PCM are coupled using the approach of Voller and Prakash [30]. To make the simulations more tractable, only laminar flow of the HTF and PCM are considered so that the axisymmetric equations of motion are applicable.

The PCM flow is assumed to satisfy the non-hydrostatic Boussinesq assumptions for conservation of mass and momentum which can be written in cylindrical coordinates as

$$\frac{1}{r}\frac{\partial(ru_r)}{\partial r} + \frac{\partial(u_z)}{\partial z} = 0 \tag{12a}$$

$$\rho_0\left(\frac{\partial u_r}{\partial t} + u_r\frac{\partial u_r}{\partial r} + u_z\frac{\partial u_r}{\partial z}\right) = -\frac{\partial p^*}{\partial r} + 2\mu\frac{\partial^2 u_r}{\partial r^2} + \mu\frac{\partial}{\partial z}\left(\frac{\partial u_r}{\partial z} + \frac{\partial u_z}{\partial r}\right) + \frac{2\mu}{r}\left(\frac{\partial u_r}{\partial r} - \frac{u_r}{r}\right) + S_r \tag{12b}$$

$$\rho_0\left(\frac{\partial u_z}{\partial t} + u_r\frac{\partial u_z}{\partial r} + u_z\frac{\partial u_z}{\partial z}\right) = -\frac{\partial p^*}{\partial z} + 2\mu\frac{\partial^2 u_z}{\partial z^2} + \mu\frac{\partial}{\partial r}\left(\frac{\partial u_z}{\partial r} + \frac{\partial u_r}{\partial z}\right) + \frac{\mu}{r}\left(\frac{\partial u_r}{\partial z} + \frac{\partial u_z}{\partial r}\right) + S_z + S_b \tag{12c}$$

Here, the force terms S_r, S_z are the momentum sinks used by the melting/solidification model of Voller and Prakash [30] and are given as

$$S_r = A_{mush}\frac{(1-\lambda)^2}{(\lambda^3+\epsilon)}u_r, S_z = A_{mush}\frac{(1-\lambda)^2}{(\lambda^3+\epsilon)}u_z \tag{13}$$

where A_{mush} is the mushy zone constant of Voller and Prakash [30] and ϵ is an arbitrarily small number to prevent division by zero in the model equation when the PCM solidifies. In their model, the liquid fraction λ is calculated as

$$\lambda = \frac{T_{liquidus} - T}{T_{liquidus} - T_{solidus}} \, . \tag{14}$$

The source term S_b is the buoyancy force given by $\rho_0\beta(T - T_0)g$, where T_0 and ρ_0 are the reference temperature and reference density used for the Boussinesq approximation and β is the coefficient of thermal expansion. Within the Boussinesq approximation, viscous heating of the fluid is taken to be negligible and so the thermal and mechanical energy equations decouple. The mechanical energy equation can be derived by taking the dot product of velocity and momentum. The thermal energy equation can be written in terms of enthalpy or temperature. ANSYS

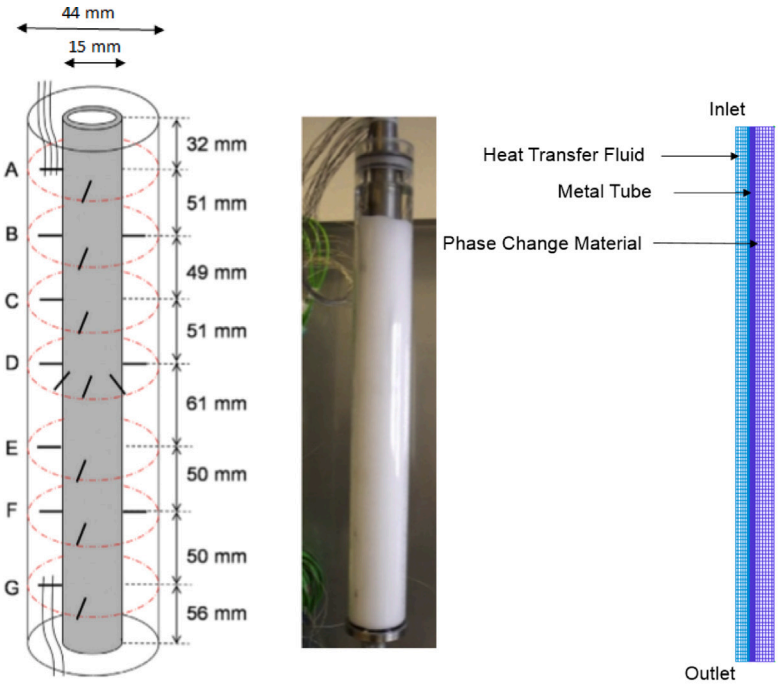

(a) Experimental setup by Longeon et al. [30] (b) Our computational domain and grid.

Fig. 2. Simulation geometry based on the laboratory experiments of Longeon et al. [31]. Panel (a) shows their experimental setup, reprinted with their permission.

Fluent, which is the code used for simulations, uses the enthalpy form of the equation, given as

$$\rho_0 \left(\frac{\partial h}{\partial t} + u_r \frac{\partial h}{\partial r} + u_z \frac{\partial h}{\partial z} \right) = \rho \dot{q}_g + \frac{1}{r} \frac{\partial}{\partial r} \left(kr \frac{\partial T}{\partial r} \right) + \frac{\partial}{\partial z} \left(k \frac{\partial T}{\partial z} \right) + S_e \quad (15)$$

where

$$S_e = \frac{\partial \rho \Delta H}{\partial t} + \nabla \cdot (\rho \vec{u} \Delta H) \, . \quad (16)$$

Here

$$\Delta H = L\lambda \quad (17)$$

is the latent heat enthalpy change for a material volume of PCM. The work associated with the momentum terms $S_r + S_z$ is

$$S_e' = \vec{u} \cdot (S_r \hat{r} + S_z \hat{z}). \quad (18)$$

Due to the small velocities, $S_e' \ll S_e$ and is neglected.

4. Simulations

The simulation geometry is chosen for validation against the laboratory results of Longeon et al. [31]. The physical configuration is shown in Fig. 2a. Due to the fact that the cylinder is oriented vertically and that the flow regime is laminar, it can be assumed that the flow is axially symmetric and the equations of motion in Section 3 are applicable. Details of the computational geometry are in Table 3a. The structured grid used for the simulations is shown as Fig. 2b. The properties of the PCM, given in Table 3c, are matched to those in Longeon et al. [31], with the exception of the sensible specific heat capacity and the density, which are different between the solid to liquid in the experiments but in the simulations are set to average values shown in Table 3b. The properties of stainless steel in the simulations are density 8030 kg/m^3, specific heat capacity 502.48 J/kg K and thermal conductivity of 16.27 W/m K, taken from the ANSYS Fluent database.

The simulations are conducted using the FVM code ANSYS Fluent. The simulation parameters are in Table 3b and d. In the phase-change model (13), the constant A_{mush} defining the mushy zone is taken to be 100,000 and it is observed that the solution is not strongly dependent on this value. The HTF inlet boundary condition is defined to be a uniform velocity of 0.01 m/s and with static temperature 53 °C. The HTF outlet boundary condition is constant gauge pressure of 0 Pa. The PCM container is set to be a no-slip, insulated (adiabatic) wall. We note that this is an idealization since the experiment performed by Longeon et al. [31] might have some heat losses, but they mention that the PCM selected had a melting temperature close to ambient temperature, which was done to minimize heat losses, at least during the charging process. The mass and momentum equations are solved using the pressure based solver with the SIMPLE algorithm used for the

Table 3
Simulation parameters used in Longeon et al. [31].

(a) Geometry of simulation domain for validation

Parameter	Value	Unit
HTF tube		
Outer radius	10	mm
Inner radius	7.5	mm
Length	400	mm
PCM container		
Inner radius	22	mm
Length	400	mm

(b) Properties of PCM used for simulation

Property	Value	Unit
ρ	820	kg/m^3
L	157	kJ/kg
C_p	2.1	kJ/kg K
μ	0.002706	kg/m s
β	0.001	1/K
$T_{solidus}$	34.95	°C
$T_{liquidus}$	35	°C
k	0.2	W/m K

(c) Properties of PCM RT35 Rubitherm as reported by [31]

Property	Value	Unit
ρ	880(s)/760(l)	kg/m^3
L	157	kJ/kg
C_p	1.8(s)/2.4(l)	kJ/kg K
μ	0.002706	kg/m s
β	0.001	1/K
T_m	35	°C
k	0.2	W/m K

(d) Properties of HTF water

Property	Value	Unit
ρ	998.2	kg/m^3
C_p	4.182	kJ/kg K
μ	0.001003	kg/m s
k	0.6	W/m K

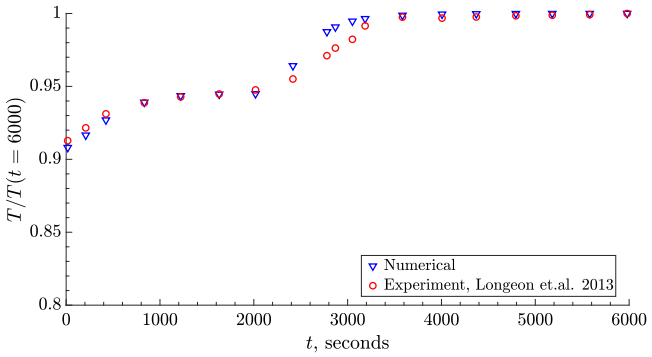

Fig. 3. Comparison of measured temperature at Point D [31] with simulation for validating simulation procedure. The maximum error is 25.8% and the RMSE error 12.2% (relative to the total temperature change of the system).

pressure velocity coupling. Pressure is discretized using the PRESTO scheme [32]. The momentum and energy equations are discretized using second order upwind schemes. The evolution in time is first order implicit, as it is sufficient for most problems [33]. The solution is initialized with zero velocity in all directions and an ambient temperature of 23 °C. The highest velocity in the domain is expected in the HTF and is twice the mean velocity, for a fully developed flow, which is 0.02 m/s.

4.1. Validation

Sensitivity of the solutions to grid resolution and time step size are examined by varying the time step size by two orders of magnitude and the number of finite volumes in the grid by a factor of approximately eight. We perform simulations with grid sizes 3446, 4696 and 27 996 and time-step sizes of 0.1 and 0.01 s. Note that our smallest grid size and largest time-step are the same order of magnitude as the grid size of 9000 and time-step of 0.5 s used by Longeon et al. [31]. The grid size of 4696 nodes and a time step of $\Delta t = 0.01$ s is sufficient to obtain grid insensitive results. Fig. 3 shows the comparison of temperature at a specific location D obtained from simulations and measured experimentally by Longeon et al. [31]. We see good agreement between the shapes of the experimental and numerical data curves.

4.2. Parametric study and results

Given the results of the validation experiments, we conclude that the simulation technique is adequate and proceeded to our parametric study. Table 4 shows the endpoint values of parameters changed and Table 5 shows the corresponding nominal dimensionless numbers. [34] mention that laminar flow is observed in vertical annular enclosures up to Grashof numbers of 10^6. The maximum Grashof number in our simulations is 199 248, thus expected to be laminar.

The simulation data base consists of 64 cases with parameters tabulated in Table 5. The simulations span a four-dimensional parameter space defined by Re_f, Pr_f, Pr_p and Gr_p with a high and low value for the first two and 4 values each for the rest. As mentioned in Section 2, we expect only a weak effect due to Re_f and Pr_f, as long as there is sufficient heat flowing into the HTF domain. It was found that $Re_f = 2090$ and $Pr_f = 5$ were more than sufficient to remove any limiting effects from the HTF. Given the expected and demonstrated weak effect of Re_f and Pr_f (provided that they are 'sufficient' to maintain the average HTF wall temperature constant), we fix their values at $Re_f = 2090$ and $Pr_f = 5$ and reduce the parameter space to include only the PCM Grashof number and Prandtl number, Gr_p and Pr_p respectively. To verify the hypothesis of (7), the melt fraction data are appropriately scaled and plotted in Fig. 4. The figure shows that all 16 cases collapse

Table 4
Physical parameters corresponding to values of dimensionless numbers in Table 5. There are a total of 64 simulations created by varying each number in Table 5 independently. For reasons of space, only the endpoint cases (numbering 16) have been shown here.

u_f	k_f	k_p	T_{in}	Re_f	Pr_f	Pr_p	Gr_p
0.01	0.1	0.1	310.125	149	42	57	24 906
0.01	0.1	0.1	324.125	149	42	57	199 248
0.01	0.1	1	310.125	149	42	6	24 906
0.01	0.1	1	324.125	149	42	6	199 248
0.01	0.8	0.1	310.125	149	5	57	24 906
0.01	0.8	0.1	324.125	149	5	57	199 248
0.01	0.8	1	310.125	149	5	6	24 906
0.01	0.8	1	324.125	149	5	6	199 248
0.14	0.1	0.1	310.125	2090	42	57	24 906
0.14	0.1	0.1	324.125	2090	42	57	199 248
0.14	0.1	1	310.125	2090	42	6	24 906
0.14	0.1	1	324.125	2090	42	6	199 248
0.14	0.8	0.1	310.125	2090	5	57	24 906
0.14	0.8	0.1	324.125	2090	5	57	199 248
0.14	0.8	1	310.125	2090	5	6	24 906
0.14	0.8	1	324.125	2090	5	6	199 248

Table 5
List of dimensionless numbers in parameter space and their values under study. Since the parameter space is four-dimensional, the total number of simulations are 64.

Re_f		Pr_f		Pr_p		Gr_p	
$Re_f 1$	149	$Pr_f 1$	42	$Pr_p 1$	57	$Gr_p 1$	24 906
$Re_f 2$	2090	$Pr_f 2$	5	$Pr_p 2$	14	$Gr_p 2$	83 020
–	–	–	–	$Pr_p 3$	8	$Gr_p 3$	141 134
–	–	–	–	$Pr_p 4$	6	$Gr_p 4$	199 248

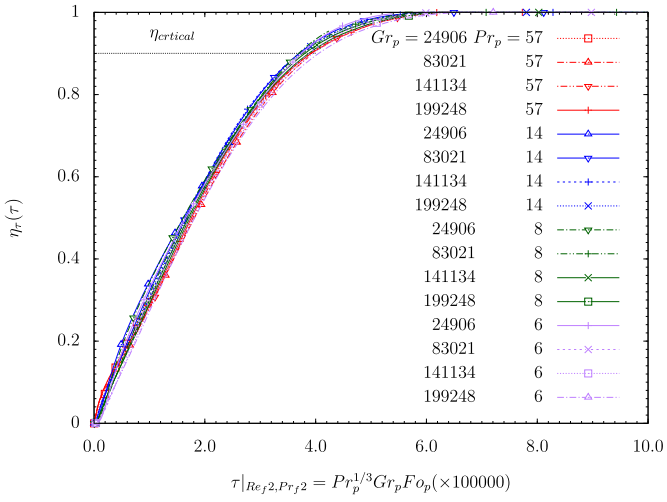

Fig. 4. The melt fraction vs dimensionless time on the parameter plane with $Re_f = 2090$ and $Pr_f = 5$. All curves collapse, indicating that the timescale defined in (7) is appropriate if Re_f is high enough and Pr_f is low enough, or if u_f and k_f are both high enough to ensure sufficient heat flow. The markers are plotted to distinguish the curves.

to almost a single curve, supporting the correlation given in (7), which is further verified by Figs. 5–7. In Fig. 5, it is observed that $Gr_p Fo_p$ collapses the data to a single curve provided that Pr_p is constant but from Fig. 6 it is apparent that the collapse also occurs for multiple values of Pr_p. Similarly, Fig. 7 shows that $Pr_p^{1/3} Fo_p$ collapses the data to a single curve provided that Gr_p is constant. These two relationships are combined in Fig. 4. For completeness, we also show a few cases in Appendix B, in which the curves do not collapse as the heat transfer is limited by the HTF, confirming our hypothesis.

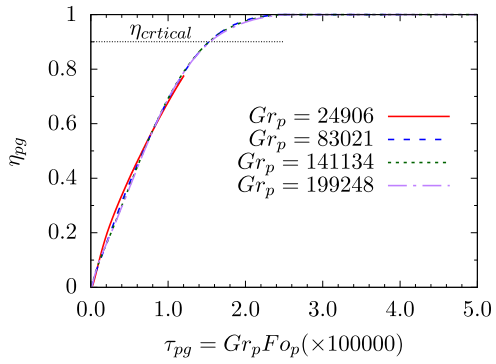

Fig. 5. The scaling of melt fraction with the Grashof number on the parameter plane with $Re_f = 2090$, $Pr_f = 5$, $Pr_p = 14$.

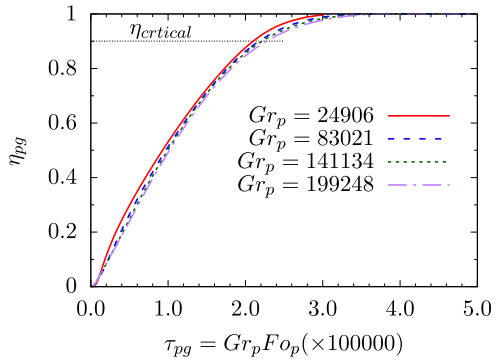

Fig. 6. Analogous to Fig. 5, but at $Pr_p = 6$.

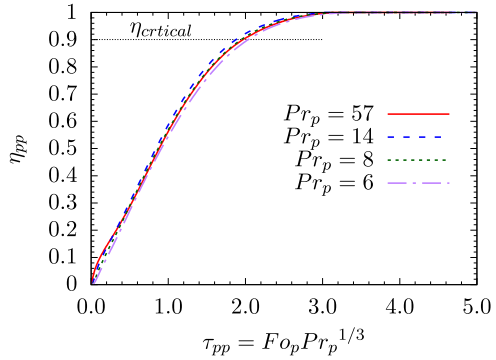

Fig. 7. Melt Fraction η as a function of Pr_p at constant $Gr_p = 199\,248$, $Pr_f = 5$ and $Re_f = 2090$. The figure shows the perfect scaling with $Pr_p{}^{1/3}$.

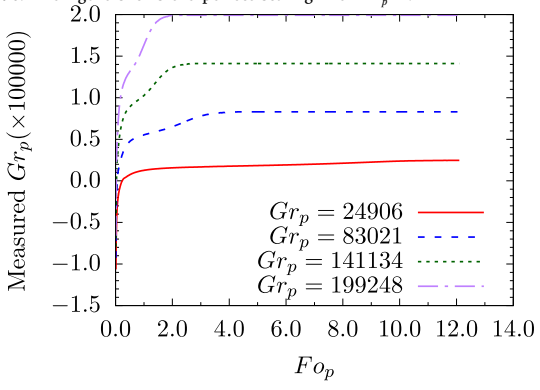

Fig. 8. Measured Gr_p as a function of non-dimensional time τ, at constant $Re_f = 2090$, $Pr_f = 5$ and $Pr_p = 6$. The plateau shows that the assumptions from Section 2.1 are justified. Negative Grashof numbers indicate that melting temperature has not been reached.

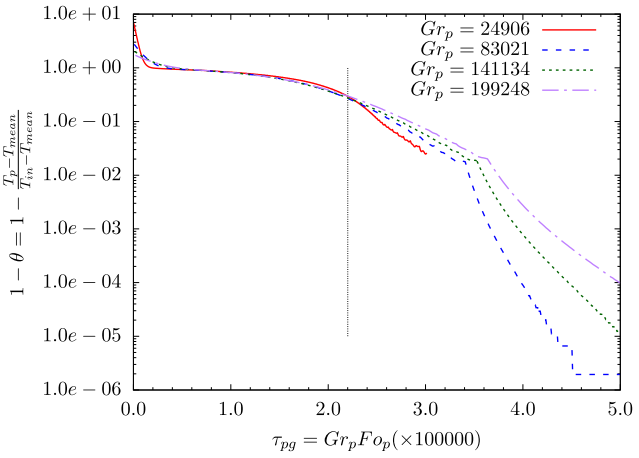

Fig. 9. Dimensionless temperature plotted as $1-\theta$ at constant $Re_f = 2090$, $Pr_f = 5$ and $Pr_p = 6$. The figure shows the existence of both linear and inverse-exponential regions as described in Sections 2.1 and 2.2. The curves collapse in the linear region. They diverge at the onset of the inverse-exponential behavior, and are displayed as straight lines due to the log-linear axes.

5. Discussion

We observe a linear region and an asymptotic region for η as predicted in Section 2, this can be seen in Fig. 4. The variation in the mean wall temperature T_{mci} is small as expected, which is observed in our simulations, see Fig. 8. The value of $\eta_{critical}$, which is of practical importance, cannot be easily determined from first principles, but can be observed in the melt fraction curve. This value is needed in order to inform whether the linear or asymptotic scaling of η with time is appropriate. From observing Fig. 4, we estimate $\eta_{critical} \approx 0.9$. The existence of the linear and inverse-exponential regions is further supported by Fig. 9, which clearly shows the collapsed curves diverging as straight lines on the onset of the inverse-exponential region, as expected on a log-linear axes. Fig. 10 shows the melt fraction and temperature contours when melting has reached $\eta_{critical}$ for cases with different Gr_p and Pr_p values. The cases have vastly different operating parameters, but we can see that there are similarities in the melt fraction profiles, for example, the shape of the remaining PCM, which has been identified in Section 2.2 as a factor in determining the shape of the melt fraction curve. This suggests that $\eta_{critical}$ might be universal for a given device, at least in the range of dimensionless numbers studied.

5.1. Effects of Gr_p and Pr_p: Discussion and implications

The Grashof number dependency given as Gr_p^1 seen in Figs. 4–6 agrees with our predictions in Section 2. This is consistent with what Jany and Bejan [28] observed by scaling analysis for mixed conduction–convection flow regimes in an enclosure with laminar flow. In this region, η varies linearly with time. Such a linear region is also observed in the experiments of Shmueli et al. [32]. On reaching $\eta_{critical}$, the curve changes shape from linear to asymptotic, as predicted in 2.2. In order to further confirm our hypothesis from 2.1, we plot the measured Grashof number in Fig. 8, which indicates that the PCM container wall temperature T_{mci} is indeed constant for the cases under consideration. Fig. 7 further confirms $Pr_p^{1/3}$ scaling obtained in Fig. 4. This scaling corresponds to the $Pr^{1/3}$ scaling observed in laminar forced convection with uniform heat flux. As explained in Section 2.1, both the temperature difference $T_{mci} - T_{mean}$ and the heat transfer rate q_{pl} are constant for majority of the time, as demonstrated by the linearity of the melt fraction curve. Due to the Boussinesq approximation, the simulated flow conserves volume, and a downward movement of volume must be matched by an upward movement. Thus, even though we cannot explain the scaling entirely, we note that the conditions in the PCM match those given in the analysis of Bejan [35, Eq 2.121],

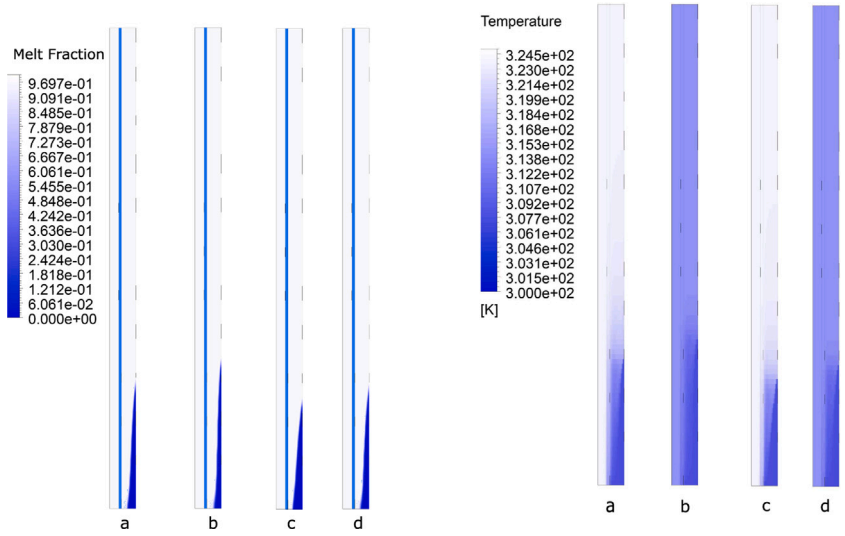

Fig. 10. Plots of liquid fraction and temperatures at time when critical liquid fraction $\eta_{critical}$ is reached. The cases 'a' and 'b' are at $Pr_p = 6$ and Gr_p of 199 248 and 83 020 respectively. The cases 'c' and 'd' are at $Pr_p = 14$ and Gr_p of 199 248 and 83 020 respectively. Notice the similarity between the shape of the solid PCM for the four different cases, even at very different case parameters. The figures are best viewed in conjunction with the geometry and grid shown in Fig. 2b.

which predicts a $Pr^{1/3}$ dependency. The simulation data was fitted using multiple regression in the region $\eta \leq \eta_{critical}$ and the fit is given as

$$\eta_\tau = (4.0912 \times 10^{-06})\ Pr_p^{0.40286}\ Gr_p^{0.9494}\ Fo_p^{1.0134} \tag{19}$$

with an R-squared value of 0.928. We note that the power coefficients closely follow those predicted from first principles. This implies that the temperature difference $T_{in} - T_{mean}$ is the most important parameter for obtaining fast heat transfer, and should be maximized. This conclusion agrees with the empirical study of Raul et al. [36] who conclude that the effect of the HTF temperature is more pronounced than other HTF parameters. The HTF inlet temperature is constrained by the application being studied. Thus, the temperature difference may be maximized by picking a PCM with a lower mean melting temperature. However, increasing this difference corresponds to a loss in quality of heat stored. The temperature T_{mean} is also expected to be an important parameter for heat transfer during discharging of the device, as it shall affect the discharging heat transfer rate. Thus, it is desirable to find an optimized value of T_{mean} that maximizes the quality stored energy and the charging and discharging rates.

6. Conclusions

The parametric performance modeling of LHTES devices is essential for their effective use. In this paper, we present a framework to analyze LHTES devices and apply it to a vertical annular geometry. We identify the system operating parameters that possibly limit heat transfer rate, namely u_f, T_{in}, k_p and k_f and hypothesize their effect on the heat transfer rate q_{pl} and the melt fraction η from first principles. We propose that given sufficient flow of HTF, the melt fraction should scale with the PCM Grashof number as Gr_p^1 and the PCM Prandtl number as $Pr_p^{(1/3)}$. We also note that the values of the HTF Reynolds number Re_f and HTF Prandtl number Pr_f are fixed such that the heat transport is not limited by the HTF.

The form of η versus time as the PCM melts has a linear region and a nonlinear region with the separation between them defined by a critical melt fraction, which, for our geometry is identified to be $\eta_{critical} \approx 90\%$. The linear region is characterized by fast and constant heat transfer rate which is a desired characteristic in LHTES devices. The nonlinear region is characterized by an asymptotic approach to fully melted and a corresponding asymptotic decrease in the heat transfer rate. Contour plots of the liquid fraction at $\eta_{critical}$ for cases with vastly different

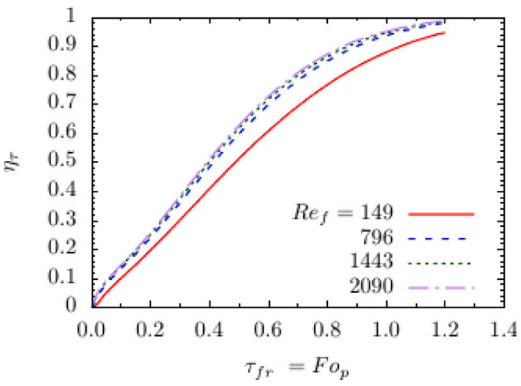

Fig. B.11. Melt Fraction as a function of Re_f at constant $Gr_p = 83\,020$, $Pr_f = 42$ and $Pr_p = 57$. The plots show that the heat transfer rate does not improve much past $Re = 800$.

parameters are observed to be similar in shape, which suggests a universality for the critical melt fraction $\eta_{critical}$. Based on this, we make the following conclusions about the design process for LHTES devices.

1. The effects of HTF velocity and thermal conductivity should be eliminated by providing sufficiently high flow and/or choosing an HTF with high conductivity. This 'sufficient' condition is indicated by the HTF tube walls approaching constant temperature. As noted in Section 4.2, the velocity and the choice of HTF fluid are somewhat easier to customize than the PCM parameters, and the HTF velocity is limited only by considerations of optimizing pumping power and reducing pipe wear. This reiterates the importance of research related to conductivity enhancement of the HTF.
2. Since the linear region in the melt fraction curve is characterized by a constant and higher heat transfer rate, it is the relevant region for operating the heat exchanger as an energy storage device.
3. The effect of the PCM Grashof number Gr_p is much stronger than the PCM Prandtl number Pr_p. In terms of selecting PCM materials and operating parameters, this indicates that varying the melting point and/or HTF inlet temperature has a stronger effect on the heat transfer rate than enhancing the thermal conductivity of the PCM. However, if the charging and discharging HTF temperatures are fixed (this is expected, since they are governed

Table A.6
Dimensional parameters that affect heat transfer rate of LHTES devices. Boxed parameters have been used for the Buckingham Pi analysis.

Properties	HTF	PCM	HTF tube	PCM container
Density	ρ_f	ρ_p	ρ_t	ρ_c
Specific heat capacity	Cp_f	Cp_p	Cp_t	Cp_c
Viscosity	μ_f	μ_p	–	–
Thermal conductivity	$\boxed{k_f}$	$\boxed{k_p}$	$\boxed{k_t}$	k_c
Volumetric expansion coefficient	β_f	$\boxed{\beta_p}$	β_t	β_c
Inlet temperature	T_{in}	–	–	–
Initial temperature			T_i	
Mean melting temperature $((T_{solidus}+T_{liquidus})/2)$	–	$\boxed{T_{mean}}$	–	–
Latent heat capacity	–	$\boxed{L}$	–	–
Time			$\boxed{t}$	
Time for solidification with under-cooling	–	$\boxed{\Delta t_s}$	–	–
Average inlet velocity/Average velocity	$\boxed{u_f}$	–	–	–
Length	–	–	$\boxed{l_t}$	$\boxed{l_c}$
Initial mass	M_f	M_p	M_t	M_c
Diameters	–	–	$\boxed{D_t}$	$\boxed{D_{ci}, D_{co}}$
Container to fluid interface area	A_f	A_p	–	–
Derived parameters				
Mean surface temperature $(\int_A TdA/A)$	–	–	–	$\boxed{T_{mci}}$
Mean heat transfer coefficient (h)	$\boxed{h_f}$	$\boxed{h_p}$	–	–
Mean melting temperature $((T_{solidus}+T_{liquidus})/2)$	–	$\boxed{T_{mean}}$	–	–

Table A.7
Other derived parameters.

Properties	HTF	PCM	HTF tube	PCM container
Thermal diffusivity $(k/\rho C_p)$	α_f	α_p	–	–
Kinematic viscosity (μ/ρ)	ν_f	ν_p	–	–
Mean volume temperature $(\int_V TdV/V)$	T_f	T_p	–	–
Heat transfer rate out of/into control volume	q_f	q_p	q_t	q_c

by the application), increasing the charging Gr_p reduces the discharging Gr_p. The melting point of the PCM should be optimized in order to satisfy both charging and discharging conditions. Hence, finding materials for which the melting point can be varied, with means such as additives or chemical composition, is indicated to be an important area for further research. This conclusion agrees with that of the review presented by Farid et al. [16]. However, we note that the thermal conductivity of PCM's is typically low and that it might be more practical to increase a PCM's thermal conductivity using additives than it is to vary its melting point.

CRediT authorship contribution statement

Kedar Prashant Shete: Simulations, Writing - original draft, Software, Editing. **S.M. de Bruyn Kops:** Methodology, Reviewing and Editing, Supervision. **Dragoljub (Beka) Kosanovic:** Reviewing and Editing, Supervision, Funding.

Declaration of competing interest

The authors declare that they have no known competing financial interests or personal relationships that could have appeared to influence the work reported in this paper.

Acknowledgment

This work was sponsored by the US Department of Energy grants DE-EE00007708 and DE-EE00008277.

Appendix A. Parameters that can affect the transient performance of an LHTES device

See Tables A.6 and A.7.

Appendix B. Eliminating HTF effects on heat transfer

In Section 2, we hypothesize that the limiting effects of HTF on the heat transfer can be greatly reduced or eliminated, given the sufficient availability of energy in the HTF. To confirm this, we perform additional simulations with two more intermediate values of $Re_f = 796$ and $Re_f = 1443$ at $Pr_f = 42$, $Gr_p = 8.302\times10^4$ and $Pr_p = 57$, the results of which are shown in Fig. B.11. Similarly, we conduct simulations of two intermediate values of $Pr_f = 8$ and $Pr_f = 6$ for the case with $Re_f = 2090$, $Pr_p = 57$ and $Gr_p = 8.302\times10^4$, results of which are shown in Fig. B.12. The plots show that the heat transfer rate does not change much beyond $Re_f = 800$ or $Pr_f = 8$, indicating sufficient availability of energy in the HTF.

Appendix C. Research flowchart

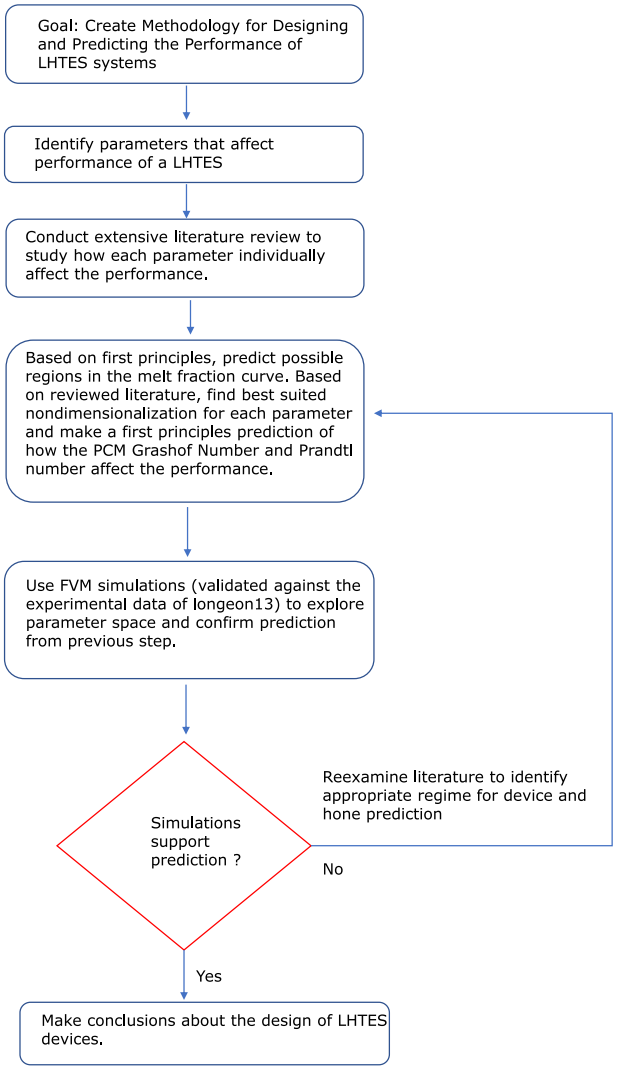

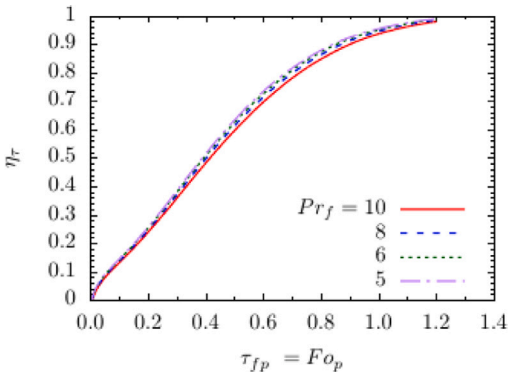

Fig. B.12. Melt Fraction as a function of four Pr_f at constant $Gr_p = 83\,020$, $Pr_p = 57$ and $Re_f = 2090$.

References

[1] P. Denholm, E. Ela, B. Kirby, Milligan. M., Role of Energy Storage with Renewable Electricity Generation, Technical Report January, National Renewable Energy Laboratory, 2010, URL http://www.osti.gov/servlets/purl/972169-1QXROM/.

[2] K. Nithyanandam, R. Pitchumani, Computational modeling of dynamic response of a latent thermal energy storage system with embedded heat pipes, J. Sol. Energy Eng. (ISSN: 0199-6231) (2013) http://dx.doi.org/10.1115/1.4024745.

[3] Kang Hu, Lei Chen, Qun Chen, Xiao-Hai Wang, Jun Qi, Fei Xu, Yong Min, Phase-change heat storage installation in combined heat and power plants for integration of renewable energy sources into power system, Energy (ISSN: 03605442) 124 (2017) 640–651, http://dx.doi.org/10.1016/j.energy.2017.02.048, URL http://linkinghub.elsevier.com/retrieve/pii/S0360544217302220.

[4] Benjamin McDaniel, Dragoljub Kosanovic, Modeling of combined heat and power plant performance with seasonal thermal energy storage, J. Energy Storage 7 (2016) 13–23.

[5] K.P. Venkitaraj, S. Suresh, Arjun Venugopal, Experimental study on the thermal performance of nano enhanced pentaerythritol in IC engine exhaust heat recovery application, Appl. Therm. Eng. (ISSN: 13594311) 137 (2017) (2018) 461–474, http://dx.doi.org/10.1016/j.applthermaleng.2018.03.062.

[6] Jun Li, Chin Hong Tam, Guohong Tian, Investigation of an HD engine thermal storage system, Energy Procedia (ISSN: 18766102) 105 (2017) 4110–4115, http://dx.doi.org/10.1016/j.egypro.2017.03.873.

[7] Maryam Arbabzadeh, Ramteen Sioshansi, Jeremiah X. Johnson, Gregory A. Keoleian, The role of energy storage in deep decarbonization of electricity production in California, Nature Commun. (ISSN: 2041-1723) (2019) (2019) 1–35, http://dx.doi.org/10.1038/s41467-019-11161-5.

[8] L. Mongibello, M. Capezzuto, G. Graditi, Technical and cost analyses of two different heat storage systems for residential micro-CHP plants, Appl. Therm. Eng. (ISSN: 13594311) 71 (2) (2014) 636–642, http://dx.doi.org/10.1016/j.applthermaleng.2013.10.026.

[9] Dheeraj Kishor Johar, Dilip Sharma, Shyam Lal Soni, Pradeep K. Gupta, Rahul Goyal, Experimental investigation and exergy analysis on thermal storage integrated micro-cogeneration system, Energy Convers. Manage. (ISSN: 01968904) 131 (2017) 127–134, http://dx.doi.org/10.1016/j.enconman.2016.10.075.

[10] Y. Cao, A. Faghri, Performance characteristics of a thermal energy storage module : a transient PCM/forced convection conjugate analysis, Int. J. Heat Mass Transfer (1991) 93–101.

[11] Lokesh Kalapala, Jaya Krishna Devanuri, Influence of operational and design parameters on the performance of a pcm based heat exchanger for thermal energy storage – a review, J. Energy Storage (ISSN: 2352-152X) 20 (2018) 497–519, http://dx.doi.org/10.1016/j.est.2018.10.024, URL http://www.sciencedirect.com/science/article/pii/S2352152X18304523.

[12] Y. Cao, A. Faghri, A study of thermal energy storage systems with conjugate turbulent forced convection, J. Heat Transfer (1992) 1019–1027, URL http://heattransfer.asmedigitalcollection.asme.org/.

[13] B. Yimer, M. Adami, Parametric study of phase change thermal energy storage systems for space application, Energy Convers. Manage. (ISSN: 0196-8904) 38 (3) (1997) 253–262, http://dx.doi.org/10.1016/S0196-8904(96)00045-3, URL https://www.sciencedirect.com/science/article/pii/S0196890496000453.

[14] Kunal Bhagat, Mohit Prabhakar, Sandip K. Saha, Estimation of thermal performance and design optimization of finned multitube latent heat thermal energy storage, J. Energy Storage (ISSN: 2352152X) (2018) http://dx.doi.org/10.1016/j.est.2018.06.014.

[15] Jaume Gasia, Jan Diriken, Malcolm Bourke, Johan Van Bael, Luisa F. Cabeza, Comparative study of the thermal performance of four different shell-and-tube heat exchangers used as latent heat thermal energy storage systems, Renew. Energy (ISSN: 18790682) (2017) http://dx.doi.org/10.1016/j.renene.2017.07.114.

[16] Mohammed M. Farid, Amar M. Khudhair, Siddique Ali K. Razack, Said Al-Hallaj, A review on phase change energy storage: Materials and applications, (ISSN: 01968904) 2004.

[17] Bechiri Mohammed, Kacem Mansouri, Analytical solution of heat transfer in a shell-and-tube latent thermal energy storage system, Renew. Energy (ISSN: 09601481) 74 (2015) 825–838, http://dx.doi.org/10.1016/j.renene.2014.09.010.

[18] Hebat-Allah M. Teamah, Marilyn F. Lightstone, James S. Cotton, Numerical investigation and nondimensional analysis of the dynamic performance of a thermal energy storage system containing phase change materials and liquid water, J. Solar Energy Eng. (ISSN: 0199-6231) (2016) http://dx.doi.org/10.1115/1.4034642.

[19] Jason Woods, Allison Mahvi, Anurag Goyal, Eric Kozubal, Adewale Odukomaiya, Roderick Jackson, Rate capability and ragone plots for phase change thermal energy storage, Nature Energy (2021) 1–8.

[20] A. Ali Rabienataj Darzi, Mahmoud Jourabian, Mousa Farhadi, Melting and solidification of pcm enhanced by radial conductive fins and nanoparticles in cylindrical annulus, Energy Convers. Manag. 118 (2016) 253–263.

[21] M. Sheikholeslami, M. Jafaryar, Ahmad. Shafee, Zhixiong Li, Simulation of nanoparticles application for expediting melting of pcm inside a finned enclosure, Physica A 523 (2019) 544–556.

[22] W.Q. Li, Z.G. Qu, Y.L. He, W.Q. Tao, Experimental and numerical studies on melting phase change heat transfer in open-cell metallic foams filled with paraffin, Appl. Therm. Eng. 37 (2012) 1–9.

[23] W.Q. Li, Z.G. Qu, Y.L. He, Y.B. Tao, Experimental study of a passive thermal management system for high-powered lithium ion batteries using porous metal foam saturated with phase change materials, J. Power Sources 255 (2014) 9–15.

[24] Z.Y. Jiang, Z.G. Qu, Lithium–ion battery thermal management using heat pipe and phase change material during discharge–charge cycle: A comprehensive numerical study, Appl. Energy 242 (2019) 378–392.

[25] Qinlong Ren, Fanlong Meng, Penghua Guo, A comparative study of pcm melting process in a heat pipe-assisted lhtes unit enhanced with nanoparticles and metal foams by immersed boundary-lattice boltzmann method at pore-scale, Int. J. Heat Mass Transfer 121 (2018) 1214–1228.

[26] K. Rathod, Banerjee Jyotirmay, Development of correlation for melting time of phase change material in latent heat storage unit, in: Energy Procedia, 2015, pp. 2125–2130, http://dx.doi.org/10.1016/j.egypro.2015.07.339, ISBN 1876-6102.

[27] G. Diarce, Campos-Celador, J.M. Sala, A. García-Romero, A novel correlation for the direct determination of the discharging time of plate-based latent heat thermal energy storage systems, Appl. Therm. Eng. (ISSN: 13594311) 129 (2018) 521–534, http://dx.doi.org/10.1016/j.applthermaleng.2017.10.057.

[28] Peter Jany, Adrian Bejan, Scaling theory of melting with natural convection in an enclosure, Int. J. Heat Mass Transfer (ISSN: 00179310) 31 (6) (1988) 1221–1235, http://dx.doi.org/10.1016/0017-9310(88)90065-8.

[29] Frank P. Incropera, David P. DeWitt, Adrienne S. Lavine, Theodore L. Bergman, Fundamentals of Heat and Mass Transfer, John Wiley & Sons, 2011.

[30] V.R. Voller, C. Prakash, A fixed grid numerical modelling methodology for convection–diffusion mushy region phase-change problems, Int. J. Heat Mass Transfer (ISSN: 00179310) (1987) http://dx.doi.org/10.1016/0017-9310(87)90317-6.

[31] Martin Longeon, Adèle Soupart, Jean François Fourmigué, Arnaud Bruch, Philippe Marty, Experimental and numerical study of annular PCM storage in the presence of natural convection, Appl. Energy (ISSN: 03062619) (2013) http://dx.doi.org/10.1016/j.apenergy.2013.06.007.

[32] H. Shmueli, G. Ziskind, R. Letan, Melting in a vertical cylindrical tube: Numerical investigation and comparison with experiments, Int. J. Heat Mass Transfer (ISSN: 00179310) (2010) http://dx.doi.org/10.1016/j.ijheatmasstransfer.2010.05.028.

[33] ANSYS Fluent, Fluent user guide, in: ANSYS FLUENT, Vol. 123, 2011, pp. 407–408, http://dx.doi.org/10.1111/j.1600-0447.2011.01711.x.

[34] Mark J. Fishbaugher, Natural convection and conduction in a vertical annulus with a concentric baffle: a numerical study, 1988.

[35] Adrian Bejan, Convection Heat Transfer, 2013, http://dx.doi.org/10.1002/9781118671627,

[36] Appasaheb K. Raul, Pratik Bhavsar, Sandip Kumar Saha, Experimental study on discharging performance of vertical multitube shell and tube latent heat thermal energy storage, J. Energy Storage 20 (2018) 279–288.